

Sediment aggradation rates in Himalayan rivers revealed through InSAR differential residual topographic phase

Jingqiu Huang¹, Hugh Denny Sinclair¹

5 ¹School of GeoSciences, University of Edinburgh, Edinburgh, EH8 9XP, UK

Correspondence to: Jingqiu Huang (jq.huang@ed.ac.uk)

SAR polarimetric backscatter amplitude analysis for dry gravel riverbeds

10 The backscatter energy (amplitude) is a critical parameter in SAR data analysis as it provides information about the surface scattering properties and is used to derive surface characteristics. Usually, higher backscatter energy results in clearer and more consistent SAR interferograms (Cloude and Papathanassiou, 1998). There are three main backscatter mechanisms: rough surface that causes diffuse scattering, vegetation that causes volume scattering and buildings that cause double-bounce.

15 SAR systems can transmit/receive horizontally (H) or vertically (V) polarized waves. There are four different polarizations in SAR backscatter signals (HH, HV, VH, VV), which are horizontal transmit and receive (HH), horizontal transmit and vertical receive (HV), vertical transmit and horizontal receive (VH), and vertical transmit and receive (VV), respectively. This configuration is relevant because different polarizations can help classify between diffuse scattering (scattering from rough surfaces), double-bounce scattering (from structures like buildings where the signal bounces twice), and volume scattering (from vegetation or other complex structures),
20 providing applications in forestry, agriculture, and urban mapping (Woodhouse, 2017). For instance, a smooth surface like water might strongly reflect horizontally polarized waves (HH), while rough surfaces might scatter vertically polarized waves (VV) more effectively (Flores-Anderson et al., 2019). The HV and VH polarizations are often used to detect biomass and forest structure since these polarizations are sensitive to volume scattering from vegetation (Mitchard et al., 2009). It is worth noting that Sentinel-1 is a dual-polarized SAR satellite, which
25 means the radar can send and receive both vertical and horizontal waves. However, the VH and HV polarized signals use the same receiving channel; therefore, VH and HV data are identical (Flores-Anderson et al., 2019). For diffuse scattering,

$$dB_{VV} > dB_{HH} > dB_{HV} , \quad (S1)$$

for double bounce scattering,

30
$$dB_{HH} > dB_{VV} > dB_{HV} , \quad (S2)$$

and for volume scattering,

$$dB_{HV} > dB_{HH} \text{ (or } dB_{VV}) , \quad (S3)$$

Due to the pebbles in riverbeds, diffuse scattering is stronger in VV polarization, while vegetated gravel bars result in stronger volume scattering in VH polarization. Figure 2 shows that when crossing the dry gravel riverbed

on river 2, in the west gravel beds exhibit relatively stronger backscatter amplitude along the VV amplitude transect compared to the east side vegetated gravel bars. In contrast, along the VH amplitude transect, in the east vegetated gravel bars show relative higher amplitude than the western gravel beds.

SAR raw data is an image, also called Single Look Complex (SLC), which preserve the phase and amplitude information from SAR backscattering signal. Each pixel in the image represents a complex number in Eq. (S4).

A complex number consists of a real part and an imaginary part, which can be thought of as a vector (a, b) in a two-dimensional plane, with the real part corresponding to the x-component and the imaginary part to the y-component. It is worth pointing out that the original SLC image is not referenced to a geographic coordinate, but is in azimuth and range project system, which is based on the SAR acquisition geometry. Azimuth is along the satellite flight path, and range is perpendicular to the satellite flight path (Loew and Mauser, 2007).

$$S = a + bi, \quad (S4)$$

Where S is a complex number represents a pixel of SAR image, a is the real part, and b is the imaginary part.

Amplitude is calculated following Eq. (S5-S8):

$$intensity = a^2 + b^2, \quad (S5)$$

$$\sigma = \sqrt{a^2 + b^2}, \quad (S6)$$

$$\sigma^0 = \sigma * \cos(\theta), \quad (S7)$$

$$dB = 10 * \log_{10}(\sigma^0), \quad (S8)$$

Where θ is the Sentinel-1 satellite SAR acquisition average incident angle. It is worth noting that Eq. (S7) is simplified only for incident angle calibration. Smooth Surfaces (like calm water bodies) tend to have low backscatter and thus lower dB values, often in the range of -25 dB to -20 dB. Vegetated areas typically show moderate backscatter, leading to dB values in the range of -20 dB to -10 dB. Urban areas with many man-made structures, generally have higher backscatter, leading to values from -15 dB to 0 dB or even higher in some cases.

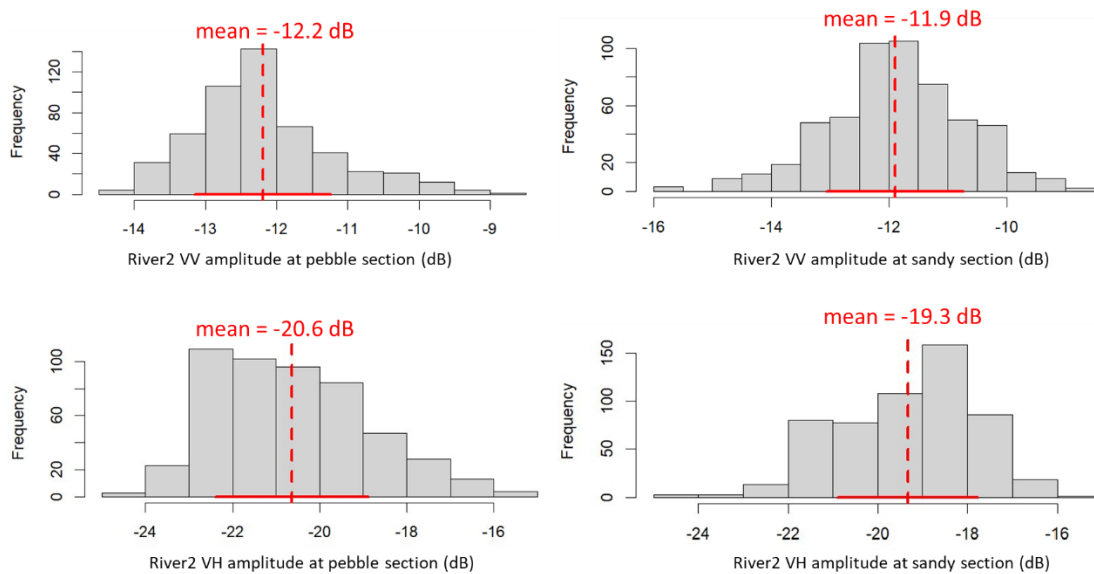


Figure S1: Descriptive statistical analysis of SAR amplitude for the pebble and sandy sections of river 2. The histograms show that the sandy section has a slightly higher mean amplitude compared to the pebble section. The VH amplitude may

be more sensitive to differences between pebble and sandy riverbeds due to the slightly larger mean difference. The standard deviations (sd) are similar across all histograms (indicated by red solid lines crossing the mean), with the following values: $sd_VV_pebble = 0.9$, $sd_VV_sandy = 1.1$, $sd_VH_pebble = 1.7$, $sd_VH_sandy = 1.5$. The standard deviations indicate that the VV amplitude shows less variability from the mean compared to the VH amplitude. The figure was generated in R Studio.

LiCSBAS processing implementation

The two most important steps in SBAS-InSAR processing are step 2 (network refinement by loop closure) for removing the low quality interferograms, and step 3 (small baseline network inversion) for inverting the unwrapped phase value into displacement. In steps 2, LiCSBAS checks the reliability of the unwrapped phase interferograms, focusing on removing unwrapping error contaminated interferograms (Morishita et al., 2020).

Phase unwrapping errors can occur when the phase difference between adjacent pixels exceeds π radians, leading to inaccuracies in the measured deformation. It groups them in sets of three images at the same pixel values Φ_{12} , Φ_{23} , and Φ_{13} , then using an equation known as the loop phase (also called the closure phase), as shown here:

$$\Phi_{123} = \Phi_{12} + \Phi_{23} - \Phi_{13} , \quad (S9)$$

When the three interferograms are free from unwrapping errors, the expected loop phase value is approximately zero, although most of the time the values are not exactly zero due to influences such as multi-look, filtering, and changes in soil moisture.

Conversely, if unwrapping errors are present in one or more interferograms, the loop phase tends to align with an integer multiple of 2π . The root mean square (RMS) value of the loop phase image serves as an indicator of the count of pixels affected by unwrapping errors within the loop. Taking the loop phase values of all pixels and calculate the RMS value, if the values exceeds a specific RMS threshold (1.5 radians in our setting) they are flagged as bad quality unwrapping interferogram and are thus excluded from further processing. It is worth noting that the loop phase evaluates unwrapped phase errors for each interferogram, not for each pixel. Based on this reason, during the 20 m resolution SBAS-InSAR processing, we applied a coherence 0.2 mask before the further processing, so the good dry river channel interferograms are not removed due to the high noise in forest areas.

In step 3, LiCSBAS convert the good quality unwrapped phase into displacement. The LiCSBAS software Morishita et al. (2020) uses singular value decomposition to solve the phase inversion equation and to get the displacement vector. LiCSBAS software also assumed linear displacement function when crossing the gaps in the network.

The application of the spatial-temporal filter in step 6 was different in 20 m and 100 m resolution processing. For the 100 m resolution, all season data was used as input to remove the residual atmospheric noise while preserving the seasonal sinusoidal non-linear feature of the surface motion time-series. A temporal filter width of 0.15 years (55 days) was set in steps 6. For 20 m resolution processing, no temporal filter was applied in step 6, as only dry season data was used, assuming no residual atmospheric noise.

$$\Phi_{displacement1} = \frac{4\pi}{\lambda} R_1 , \quad (S10)$$

$$\Phi_{displacement2} = \frac{4\pi}{\lambda} R_2 , \quad (S12)$$

$$\Delta\Phi_{displacement} = \frac{4\pi}{\lambda} (R_2 - R_1) , \quad (S13)$$

Finally, we converted the line-of-sight (LOS) velocity values to vertical velocity values based on the equation below, which assumes that all observed deformations are vertical.

$$V_{\text{vertical}} = \frac{V_{\text{los}}}{\cos 38.8^\circ}, \quad (\text{S14})$$

Where 38.8° is the Sentinel-1 satellite SAR acquisition average incident angle (Fig. S3). The incident angle is the angle between the radar beam and the vertical line perpendicular to the Earth surface.

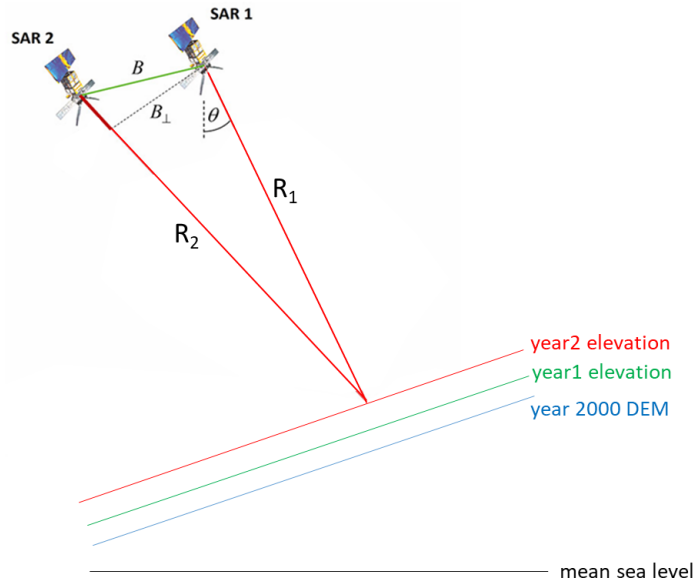


Figure S2: Geometry of satellite SAR acquisition for multi-temporal InSAR processing purposes, with parameter of perpendicular baseline (B_{\perp}), incident angle (θ), and distance between satellite and earth surface (R). Modified from Zhao et al. (2023).

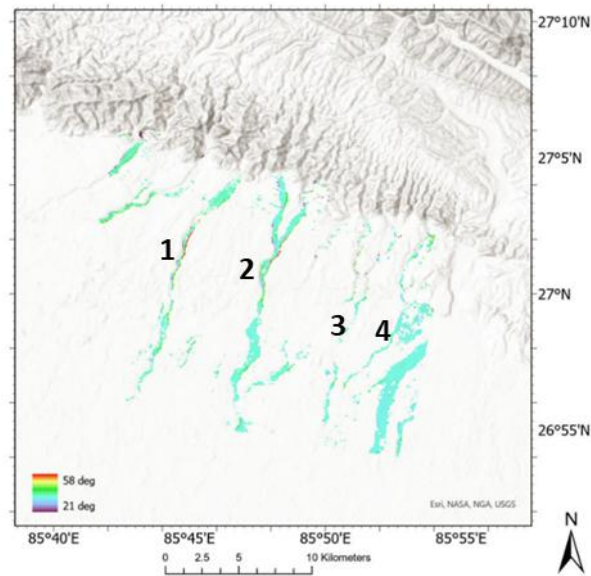


Figure S3: SAR incident angle map acquired on date 29/11/2019, descending frame sourced from the Alaska Satellite Facility (ASF), which illustrates the direction of the radar sensor looking direction. The local incidence angle, measured in

degrees, is the angle between the incoming radar beam and the normal to the local surface. The average angle is consistently 38.8° along river channels. This angle is used in Eq. (S14) to convert the Line of Sight (LOS) velocity to vertical velocity.

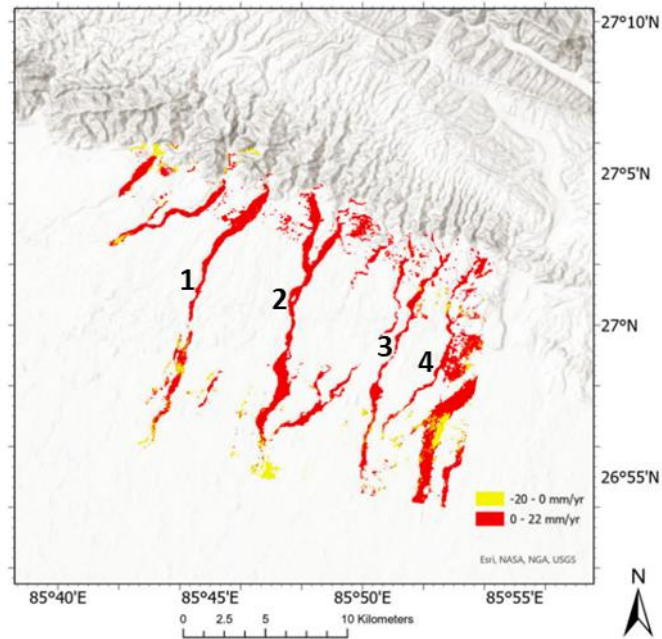


Figure S4: The spatial distribution of riverbed elevation changes from 2016 to 2021. Areas with values above zero are shown in red, indicating areas of sediment deposition. Areas with values below zero are shown in yellow, indicate regions affected by sediment erosion or land subsidence.

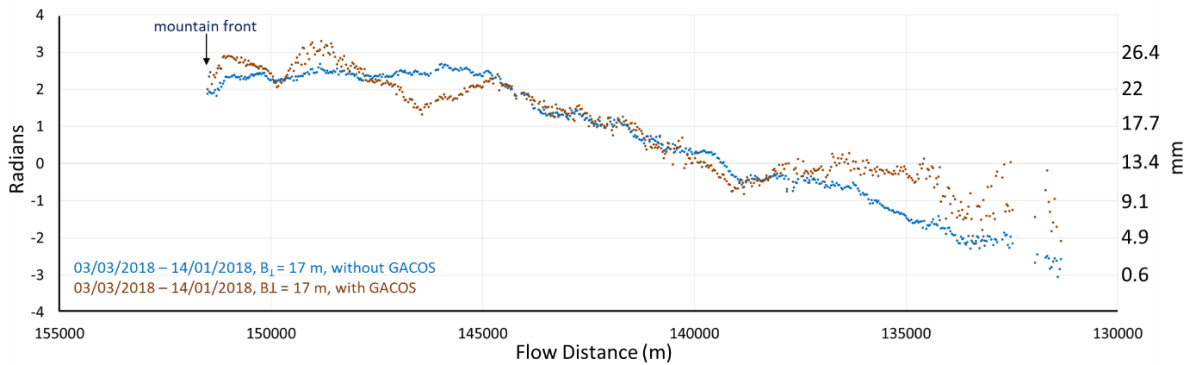


Figure S5: Residual topographic phase changes along river 2, with and without atmospheric correction. The filtered, unwrapped phase values with GACOS (brown curve), comparing without GACOS correction (blue curve). The GACOS correction revealed a couple of delays in phase values near the mountain front, while the overall trend of the phase values remained the same. This indicates a minor atmospheric noise effect.

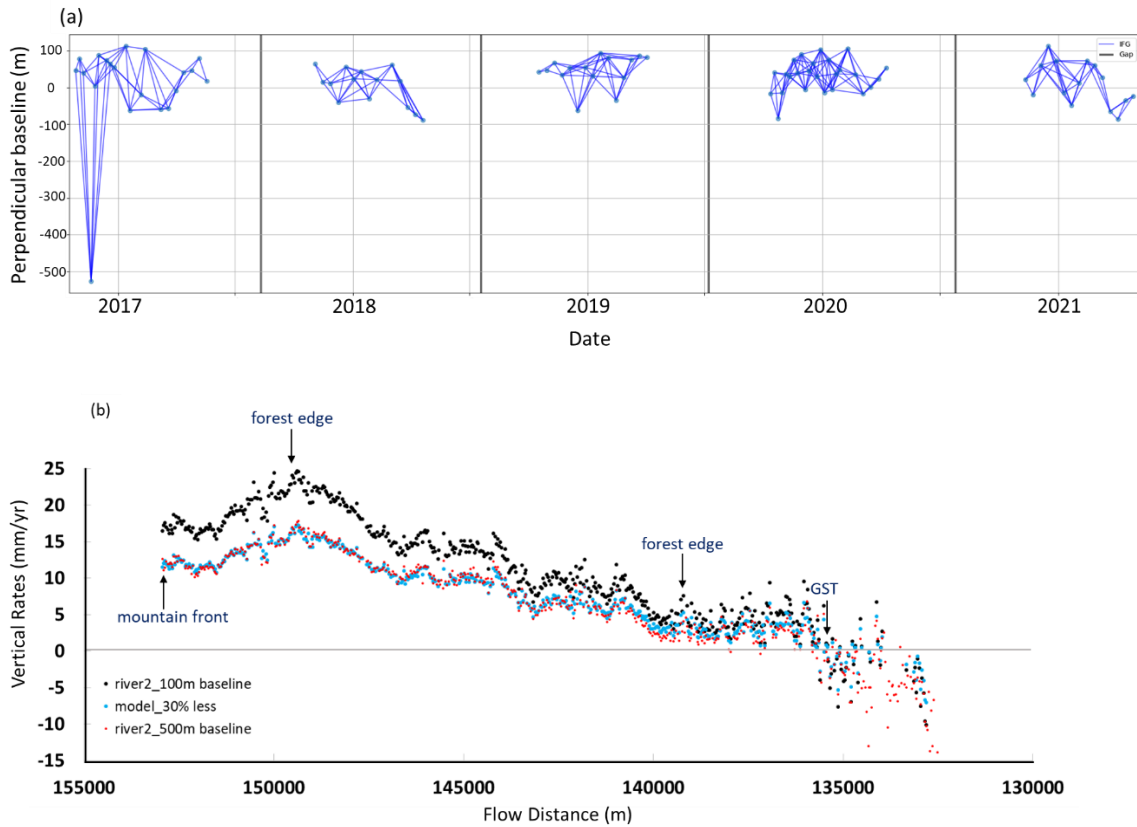


Figure S6: (a) A network of 20 m resolution interferograms was added with 7 additional interferograms in 2016, each with an over 500 m baseline. (b) The red-coloured result from the interferogram network in (a). The black-coloured result represents baselines constrained within a ± 100 m range, as illustrated in Figure 8. Both vertical rate curves exhibit the same trend: a 'V-shaped' subsidence between the mountain front and the forest edge, gradually decreasing towards gravel-sand transition, and finally fluctuating around zero. The vertical exaggeration in this plot is 250,000. The red curve is approximately 30% lower than the black curve due to the change in the topographic phase ambiguity caused by the 500 m baseline. Blue curve is modelled 30% less of the black curve.

Date	Baseline (m)	Date	Baseline (m)	Date	Baseline (m)	Date	Baseline (m)	Date	Baseline (m)	Date	Baseline (m)
20160921	0	20170113	111.6	20180102	23.5	20190109	30.4	20200104	-13.7	20210110	-14.3
20161027	46.7	20170119	-62.0	20180114	43.6	20190121	93.6	20200110	74.9	20210122	-48.4
20161102	77.8	20170206	-19.8	20180126	-30.4	20190202	81.1	20200116	-6.0	20210203	12.0
20161108	39.0	20170212	103.9	20180207	21.0	20190214	-34.5	20200122	37.0	20210215	72.3
20161126	3.8	20170308	-60.1	20180303	61.2	20190226	26.6	20200128	48.2	20210227	60.6
20161202	87.2	20170320	-56.7	20180315	17.7	20190310	75.6	20200209	104.9	20210311	27.3
20161214	74.0	20170401	-8.7	20180327	-53.8	20190322	85.9	20200221	34.7	20210323	-64.7
20161220	63.9	20170413	40.4	20180408	-74.0	20190403	81.5	20200304	-17.7	20210404	-86.5
20161226	54.1	20170425	46.0	20180420	-89.2	20191012	-16.8	20200316	0.5	20210416	-35.3
		20171103	63.5	20181017	41.6	20191018	40.4	20200328	22.5	20210428	-23.3
		20171115	14.4	20181029	46.9	20191024	-83.8	20200409	53.1		
		20171127	11.0	20181110	66.4	20191030	-15.0	20201111	21.3		
		20171209	-40.3	20181122	33.1	20191105	36.6	20201123	-19.9		
		20171221	55.6	20181204	53.1	20191111	29.7	20201205	60.2		
				20181216	-62.9	20191117	75.6	20201217	112.0		
				20181228	54.5	20191123	38.9	20201229	72.1		
						20191129	89.9				
						20191205	-6.2				
						20191211	45.2				
						20191217	66.0				
						20191223	29.4				
						20191229	102.6				

Table S1: List of SAR images and their associated baselines used for river sediment aggradation mapping. The perpendicular baselines are relative to the reference SAR image dated 2016-09-21.

References

- 150 Cloude, S. R. and Papathanassiou, K. P.: Polarimetric SAR interferometry, *IEEE Transactions on geoscience and remote sensing*, 36, 1551-1565, 1998.
- Flores-Anderson, A. I., Herndon, K. E., Thapa, R. B., and Cherrington, E.: *The SAR handbook: Comprehensive methodologies for forest monitoring and biomass estimation*, 2019.
- Loew, A. and Mauser, W.: Generation of geometrically and radiometrically terrain corrected SAR image products, *Remote Sensing of Environment*, 106, 337-349, 2007.
- 155 Mitchard, E. T., Saatchi, S. S., Woodhouse, I. H., Nangendo, G., Ribeiro, N., Williams, M., Ryan, C. M., Lewis, S. L., Feldpausch, T., and Meir, P.: Using satellite radar backscatter to predict above-ground woody biomass: A consistent relationship across four different African landscapes, *Geophysical Research Letters*, 36, 2009.
- Woodhouse, I. H.: *Introduction to microwave remote sensing*, CRC press 2017.
- 160 Zhao, Z., Wan, P., Huang, N., Shan, C., Hu, Z., Li, Y., and Zhang, J.: *Interferometric Synthetic Aperture Radar Phase Composition Analysis and Simulation*, *Sensors & Materials*, 35, 2023.